Journal of
Materials Chemistry A

Accepted Manuscript

This article can be cited before page numbers have been issued, to do this please use: C. Chen, J. Wu, W. Huang, Y. Chang, B. Tsai, Y. Hsiao, C. Chang and C. Chen, *J. Mater. Chem. A*, 2017, DOI: 10.1039/C7TA02617J.

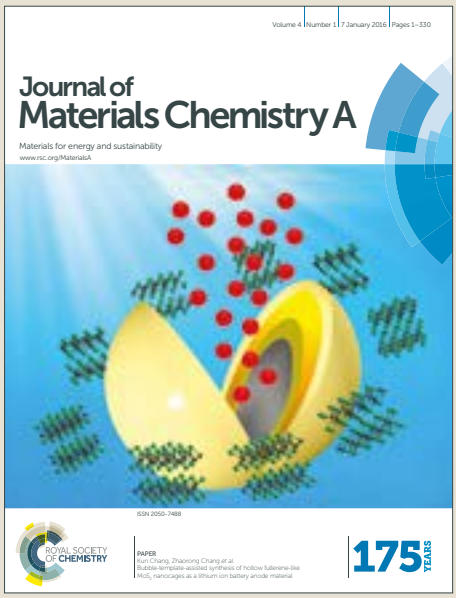

ROYAL SOCIETY OF CHEMISTRY

rsc.li/materials-a

View Article Online
DOI: 10.1039/C7TA02617J

Journal of Materials Chemistry A

PAPER

Simple mono-halogenated perylene diimides as non-fullerene electron transporting materials in inverted perovskite solar cells with ZnO nanoparticle cathode buffer layer

Received 00th January 20xx,
Accepted 00th January 20xx

DOI: 10.1039/x0xx00000x

www.rsc.org/

Jhao-lin Wu,[a] Wen-Kuan Huang,[b] Yu-Chia Chang,[b] Bo-Chou Tsai,[b] Yu-Cheng Hsiao,[b] Chih-Yu Chang,[*b] Chin-Ti Chen,[*c] and Chao-Tsen Chen[*a]

We have synthesized and characterized three perylene diimides, i.e., **X-PDI**, **X** = **H**, **F**, or **Br**. These three compounds are tested for the substitution of [6,6]-phenyl C61 butyric acid methyl ester ($PC_{61}BM$) in inverted perovskite solar cells (PVSCs). Although efficiency of PDI derivative-based conventional PVSCs is as high as 17.6% (*J. Mater. Chem. A*, **2016**, *4*, 8724), corresponding performance of inverted PVSCs is still lagged behind and the improvement is necessary. For electron accepting (from $CH_3NH_3PbI_3$ perovskite) and electron transporting properties of the materials, The UV-visible absorption spectroscopy, electrochemical cyclic voltammetry, direct current conductivity, space-charge limited current (SCLC) electron mobility, atomic force microscopy (AFM) surface morphology, and photoluminescence (PL) spectroscopy gauging charge-trap have been studied. The HOMO/LUMO energy levels are 5.94/4.00, 5.83/3.96, 6.00/3.97, and 5.48/3.73 eV for **H-PDI**, **F-PDI**, **Br-PDI**, and $PC_{61}BM$, respectively. Direct current conductivities of **H-PDI**, **F-PDI**, **Br-PDI**, and $PC_{61}BM$ are 8.71×10^{-8}, 1.18×10^{-9}, 2.2×10^{-6}, and 8.42×10^{-6} S cm^{-1}, respectively. The SCLC electron mobility of **H-PDI**, **F-PDI**, **Br-PDI**, and $PC_{61}BM$ are 1.12×10^{-4}, 8.31×10^{-6}, 1.08×10^{-3}, and 5.00×10^{-3} S cm^{-1}, respectively. PL spectroscopy of $CH_3NH_3PbI_3$ perovskite provides emission wavelength peaked at 781 nm, which is the same as perovskite layer covered with a thin film of **H-PDI** or **F-PDI**. However, the emission wavelength is blue-shifted to 773-774 nm when the perovskite layer was covered with a thin film of **Br-PDI** or $PC_{61}BM$. By UV-visible absorption spectroscopy, solution (in chloroform) solubility was determined as 1.2×10^{-2}, 8.7×10^{-2}, and $> 10^{-1}$ mol L^{-1} for **F-PDI**, **H-PDI**, and **Br-PDI**, respectively. As thin film sate, UV-visible absorption spectroscopy indicated the extent of molecular aggregation is **F-PDI** >> **H-PDI** > **Br-PDI**, which is consistent with the AFM-estimated root-mean-square roughness of **F-PDI** > **H-PDI** > **Br-PDI** ~ $PC_{61}BM$. Without solution processed ZnO NP cathode buffer layer (CBL), power conversion efficiency (PCE) of **H-PDI**, **F-PDI**, **Br-PDI**, and $PC_{61}BM$ PVSCs is ~1%, ~0%, 3.2%, and 4.1%, respectively. With the ZnO NP CBL, PCE is ~7.8%, ~0%, 10.5%, and 11.1% for **H-PDI**, **F-PDI**, **Br-PDI**, and $PC_{61}BM$ PVSCs, respectively. Through this study, we have demonstrated that the simple mono-bromine substituted perylene diimide (**Br-PDI**), which is solution processable and is potential for a non-fullerene electron accepting and electron transporting material in inverted PVSCs.

Introduction

Since 2013, there has been great development in the field of perovskite solar cells (PVSCs), which have the advantages of low cost, simple fabrication and high efficiency.[1–4] To date, the certified maximum power conversion efficiency (PCE) of perovskite solar cells has reached 21.1%.[5] Based on either mesoscopic or planar device architectures, PVSCs are typically composed of a light harvesting perovskite layer sandwiched between an electron transport layer (ETL) and hole transport layer (HTL). For an inverted construction of planar PVSCs, the conventional transport layers are poly (3,4-ethylenedioxythiophene) polystyrene sulphonate (PEDOT:PSS) and [6,6]-phenyl C61 butyric acid methyl ester ($PC_{61}BM$) as HTL and ETL, respectively.[6] In addition to the compatible solution process with perovskite material, polymer PEDOT:PSS has been widely used as an HTL for inverted PVSCs due to its good conductivity (0.014 S cm^{-1})[7] and small work function of 5.0 eV. On the other hand, C_{60} fullerene derivative $PC_{61}BM$ is usually chosen as solution processed ETL because (i) the high conductivity (0.016 mS cm^{-1})[7] or impressive electron mobility (space-charge limited mobility 5×10^{-3} cm^2 V^{-1} S^{-1})[8] which is expected to reduce the current density (*J*)–voltage (*V*) hysteresis with respect to the scan direction because of the balanced charge carrier of devices; (ii) a relatively deep lowest unoccupied molecular orbital (LUMO) energy level of -4.15 eV[9] which is energetically favourable for extracting electron from perovskite exciton. Due to these good physical features, few other organic materials are better than $PC_{61}BM$ as ETL for inverted PVSCs. However, $PC_{61}BM$ is not photochemically stable and it is prone to aggregate resulting a thin film with poor

[a] Department of Chemistry, National Taiwan University, Taipei, Taiwan 10617, R.O.C. (*E-mail: chenct@ntu.edu.tw)
[b] Department of Materials Science and Engineering, Feng Chia University, Taichung, Taiwan 40724, R.O.C. (*E-mail: changcyu@fcu.edu.tw)
[c] Institute of Chemistry, Academia Sinica, Taipei, Taiwan 11529, R.O.C. (*E-mail: chintchen@gate.sinica.edu.tw)

View Article Online
DOI: 10.1039/C7TA00617J

morphology that impairs the physical feathers mentioned above. Therefore, non-fullerene type ETLs, particularly those suitable for inverted PVSCs, are highly demanded.

The perylene diimide (PDI) compounds are n-type semiconductors with relatively low LUMO energy levels in a range of 3.5-4.3 eV[10,11] due to the electron affinity of its imide parts. Their high electron mobility (space-charge limited mobility of 0.2 ~ 1.3 $cm^2 V^{-1} S^{-1}$)[12-14] and conductivity (4.4×10^{-2} ~ 3.3×10^{-3} S cm^{-1})[15,16] originate from the rigid and planar π-skeleton, which are prone to ordered molecular packing. In addition to three reports about bis(N,N'-dimethylaminopropyl)perylene diimide (N-PDI)[17], bis(N,N'-2,4-difluorophenyl)perylene diimide (dFPh-PDI)[18], and N,N'-Bis(3-(dimethylamino)propyl)-5,11-dioctylcoronene-2,3,8,9-tetracarboxdiimide[19] as ETL in conventional PVSCs, there are only two reports about inverted PVSCs, which are more pertinent to the study herein. They are *N,N*-dioxide of bis(N,N'-dimethylaminopropyl)perylene diimide (PDINO)[20,21] and 1,1'-di-perylene diimide (diPDI).[22] The inverted configuration of PVSCs are ITO/PEDOT:PSS/$CH_3NH_3PbI_{3-x}Cl_x$/$PC_{61}BM$/PDINO/Ag and ITO/PEDOT:PSS/$CH_3NH_3PbI_3$/diPDI:DMBI/TiO_2/Al, respectively. In the case of PDINO PVSC, PCE as high as 14.0% was achieved, although PDINO was actually used as a cathode buffer layer (CBL) or cathode interlayer (CIL) instead of ETL.[21] In the case of diPDI PVSC, PCE as high as 10.0% was achieved but an n-type dopant (1,3-dimethyl-2-phenyl-2,3-dihydro-1H-benzoimidazole: DMBI) has to be included in the ETL. Otherwise, PCE of 7.1% was the best result without DMBI dopant in diPDI ETL.

There are a number of literature reports having ZnO as CBL or CIL in polymer-based bulk heterojuction conventional solar cells.[23-25] In addition to the low cost and ambient stability of ZnO, a combination effect of hole-blocking (reducing charge recombination), enhancing election extraction (or selection), preventing diffusion of cathode metal into active layer through the interspace of incomplete ETL, and the optical spacer effect has been attributed to the improvement of the device performance. To our surprise in surveying literature, only three of our previous reports have mentioned solution processed ZnO nanoparticles (NPs) as CBL or CIL in a series of inverted PVSCs.[26-28] Potentially, there could be an interdissolving problem of the perovskite material when applying ZnO nanoparticles (NPs) solution (in ethanol) by a solution process, if the ETL thin film has an low surface coverage and forms serious aggregate with large interspace between aggregate domains. The solvent of ZnO NPs may leak through the ETL thin film reaching perovskite layer underneath and may generate a straight up tunnel facilitating the direct contact of deposited cathode metal.

In this report, we demonstrate two structure simple mono-halogen-substituted **X-PDI**, i.e., **F-PDI** (**X** = **F**) and **Br-PDI** (**X** = **Br**), in addition to the parent **H-PDI** (**X** = **H**) (Figure 1), to replace the commonly used $PC_{61}BM$ as ETL in inverted $MAPbI_3$ (MA: methylammonium) PVSCs. Adding ZnO NPs as a CBL or CIL on the top of the ETL, we have successfully fabricated PVSCs with improved PCEs. A respectable PCE of 10.5% has been reached by **Br-PDI**/ZnO NP PVSC, which is comparable with 11.1% of PVSCs based on $PC_{61}BM$/ZnO NP. Whereas PVSCs based on **H-PDI** are inferior to **Br-PDI** ones, **F-PDI** PVSCs exhibit virtually no photovoltaic effect regardless ZnO NPs. We have conducted a series of experiments to find out the reasons why **Br-PDI** is better than **H-PDI** and why **F-PDI** is so poor for PVSCs.

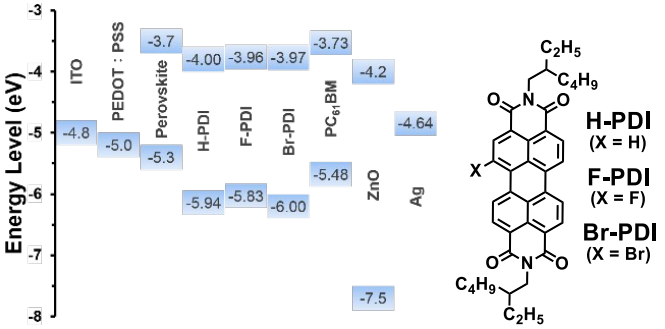

Fig 1 Energy levels of each layer alignment of PVSCs (left) and chemical structures of **X-PDI** (right).

Results and discussion

Synthesis and characterization

Each **of X-PDI** was prepared consecutively in a three-step synthetic procedure (Scheme 1). The synthesis started from the imidization of a commonly available commercial product of perylene-3,4,9,10-tetracarboxylic dianhydride. From the reaction with 2-ethyl-1-hexylamine under refluxing condition in *N*-methyl-2-pyrrolidione (NMP), **H-PDI** was obtained with near quantitative isolation yields (97%). In fact, **H-PDI** is a literature known compound.[29-31] Following the same literature procedure, **Br-PDI** was afforded from a room temperature reaction of **H-PDI** and bromine in dichloromethane, although 34% was the best isolation yields after the purification by column chromatography. **F-PDI** is a previously unknown compound and its synthetic procedure was modified from a literature report of a 1,7-difluoro-substituted perylene diimide derivative.[32] Synthetic details and the characterization data of **F-DPI** can be found in the section of experimental.

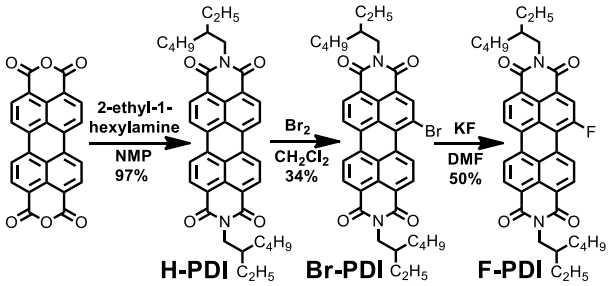

Scheme 1 consecutive synthesis of three **X-DPI** compounds.

Absorption spectroscopic properties

Figure 2 shows the UV-visible absorption spectra for both **X-PDI** chloroform solution (10^{-5} mol L^{-1}) and spin-coated thin film. Their data are summarized in Table 1. The spectra (300-600 nm) of **X-PDI** in solution mainly consist of a π-π* electronic transitions associated with a series of characteristic vibronic

structures.[33, 34] They are 0-0, 0-1, 0-2, and maybe 0-3 transitions with absorption λ_{max} at 520-525, 484-489, 454-459, 430-433 nm, respectively. The absorption spectra of the spin-coated thin film

all show broadening, splitting, and red-shifting absorption bands, of which relative intensity of the vibronic structures is quite different from those of solution spectra. All these changes of spectroscopic feature indicate a significant molecular interaction of **X-PDI** taking place in solid state (as thin film). In addition, **F-PDI** has a most intense absorption band around 633 nm in Figure 2b, which can be ascribed to the strong molecular interactions (π-π, F-π, F-F interactions) of **F-PDI** in solid state. Moreover, the high-rise base line observed in the spectrum of **F-PDI** thin film can be attributed to the scattering of near infrared and the long wavelength of visible light, which is consistent with the pronounced inhomogeneity of **F-PDI** thin film. On the other hand, molecular interaction of **X-PDI** also reflects in solution solubility. Based on the Beer's law of absorption spectroscopic measurement, **F-PDI** has the worst solubility (1.2×10^{-2} mol L^{-1}) followed by **H-PDI** (8.7×10^{-2} mol L^{-1}), which is relatively better than **F-DPI**. The solubility of **Br-PDI** (> 10^{-1} mol L^{-1}) is at least an order of magnitude higher than **F-PDI**. In this regard, **F-PDI** has the strongest molecular interaction in solid state, whereas **Br-PDI** has the weakest molecular interaction in solid state. The bulky bromine substituent inhibits the π-π stacking of **Br-PDI** in solid state and a higher solubility observed for **Br-PDI** than **H-PDI** in solution. Considering the solubility and molecular interaction, the homogeneity or quality of solution-processed **Br-PDI** thin film should be better than that of **H-PDI** or **F-PDI.** Such speculation has been verified in the AFM study (see the results and discussion of thin film surface morphology later).

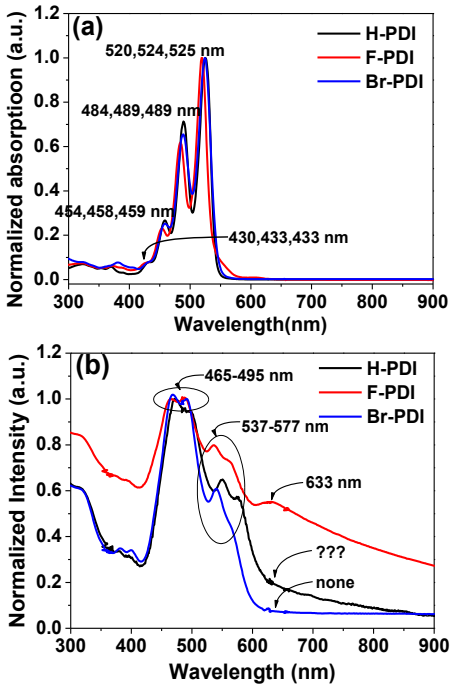

Fig 2 UV-Vis absorption spectra of **X-PDI** in chloroform solution (a) and as thin film (b).

Table 1 Summary of the UV-visible absorption spectroscopy of **X-PDI**

	Solution			Film		
	λ_{max} [nm]	λ_{onset} [nm]	E_g^{op} [eV][a]	λ_{max} [nm]	λ_{onset} [nm]	E_g^{op} [eV][a]
H-PDI	525	541	2.29	471	637	1.94
F-PDI	520	545	2.28	467	662[b]	1.87[b]
Br-PDI	524	544	2.28	469	610	2.03
$PC_{61}BM$	510	630	1.97	530[b]	710[b]	1.75[b]

[a] optical energy gap (E_g^{op}) corresponding to absorption onset wavelength. [b] estimated value.

Table 2 Cyclic voltammetry data and HOMO/LUMO energy levels of **X-PDI** and $PC_{61}BM$.

	Solution			Film		
	$E_{1/2}^{red1}$ [V]	E_{LUMO} [ev]	E_{HOMO}^{op} [ev]	$E_{1/2}^{red1}$ [V]	E_{LUMO} [ev]	E_{HOMO}^{op} [ev]
H-PDI	-1.05	-4.05	-6.34	-1.10	-4.00	-5.94
F-PDI	-1.02	-4.08	-6.36	-1.14	-3.96	-5.83
Br-PDI	-1.00	-4.10	-6.38	-1.13	-3.97	-6.00
$PC_{61}BM$	-1.08	-4.02	-5.99	-1.37	-3.73	-5.48

a $E_{1/2}^{red1}$ is the half-wave potential of the first reduction; $E_{LUMO} = -(E_{1/2}^{red1} + 5.10)$; $E_{HOMO}^{op} = E_{LUMO} - (E_g^{op}$ in Table 1).

Cyclic voltammetry - energy level determination

The electrochemical properties of **X-PDI** and $PC_{61}BM$ were studied by cyclic voltammetry (CV). The corresponding electrochemical data are summarized in Table 2. The cyclic voltammograms of **X-PDI** and $PC_{61}BM$ measured in solution (dichloromethane) and as thin film coated on electrode are shown in Fig. 3.

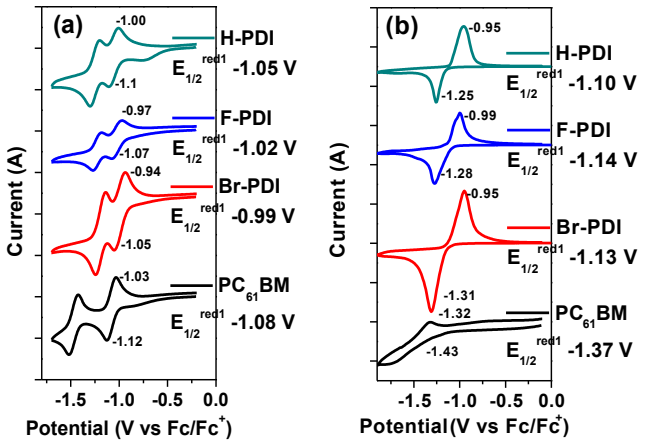

Fig 3 Cyclic voltammetry of **X-PDI** in chloroform solution (a) and as thin film (b).

As can be seen in Fig. 3a, all voltammograms of **X-PDI** or $PC_{61}BM$ in dichloromethane show two reversible or semi-reversible reduction signals in the negative potential around -1.0 V, relative to the oxidation potential of ferrocene (Fc → Fc^+). Based on the solution first reduction potential ($E_{1/2}^{red1}$), all **X-PDI** have a slightly weaker electron affinity than that of $PC_{61}BM$, indicating three **X-PDI** reported here are potential as electron acceptor like $PC_{61}BM$ for perovskite material. Here, we have

found that the mono fluorine or bromine substituent little affects the reduction potential of **H-PDI**. However, in the thin film measurement (Figure 3b), there seems only one reduction signal of three **X-PDI** and $PC_{61}BM$ in voltammograms around -1.10~-1.14 V and they are all less negative than -1.37 V of $PC_{61}BM$. Just considering the energy level of LUMO or $E_{1/2}^{red1}$ in solid state, all **X-PDI** are better electron acceptor than $PC_{61}BM$ for perovskite material. Comparing solution and thin film data, it is interesting to note that the shifting of energy levels is more pronounced on HOMO than on LUMO energy levels. Moreover, the shifting of HOMO energy level is **F-PDI > H-PDI > Br-PDI**, which is consistent with the order of molecular interaction and solubility found for **X-PDI** series.

Direct current conductivity of X-PDI and $PC_{61}BM$

The DC (direct current) conductivity (σ_0) can be determined from the slope of the current-voltage (I–V) plot. Figure 4 shows the I–V characteristics of ITO/**X-PDI** or $PC_{61}BM$/Al devices. The thicknesses of the thin films are 200, 260, 250, and 280 nm for $PC_{61}BM$, **H-PDI**, **F-PDI**, and **Br-PD**, respectively. The corresponding DC σ_0s of $PC_{61}BM$, **H-PDI**, **F-PDI**, and **Br-PDI** are 8.42×10^{-6}, 8.71×10^{-8}, 1.18×10^{-9}, and 2.2×10^{-6} S cm^{-1}, respectively. Among **X-PDI**, **Br-PDI** has the highest DC σ_0, which is in the same order of magnitude comparing with $PC_{61}BM$. Therefore, it can be expected that the charge carriers generated in the $MAPbI_3$ layer will be more efficiently transported through $PC_{61}BM$ or **Br-PDI** than **H-PDI** or **F-PDI**. On the other hand, among **X-PDI**, **F-PDI** has the lowest DC σ_0, which can be attributed to its poor thin film morphology and the relatively low solubility in solution.

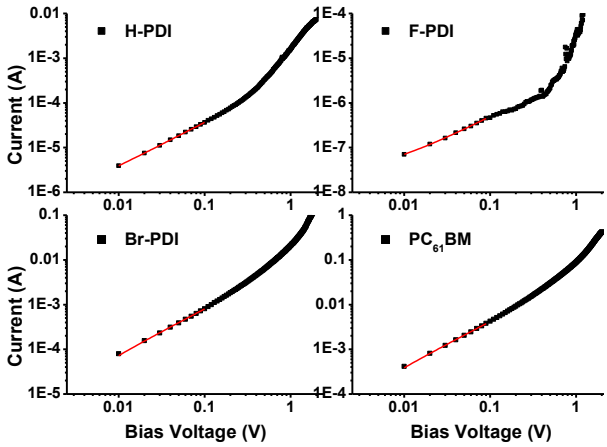

Fig 4 I–V characteristics of ITO/**X-PDI** or $PC_{61}BM$/Al devices.

Table 3 SCLC electron mobilities of **X-PDI** and $PC_{61}BM$ with and without ZnO NP.

	w/o ZnO NP μ_e (cm^2 V^{-1} s^{-1})	w/ ZnO NP μ_e (cm^2 V^{-1} s^{-1})
H-PDI	1.12×10^{-4}	4.57×10^{-4}
F-PDI	8.31×10^{-6}	1.29×10^{-5}
Br-PDI	1.08×10^{-3}	1.84×10^{-2}
$PC_{61}BM$	5.00×10^{-3}	2.54×10^{-2}

Space charge limited current - electron mobility

The charge carrier transport of **X-PDI** and $PC_{61}BM$ ETLs was studied by the space-charge limited current (SCLC) approach. The electron mobilities determined from a series of electron–dominated devices are summarized in Table 3. The electron–dominated devices studied herein are ITO/ZnO/**X-PDI** (or $PC_{61}BM$)/Ca/Al and ITO/ZnO/**X-PDI** (or $PC_{61}BM$)/ZnO NP/Ca/Al, with and without ZnO NP layer, respectively.

Figure 5a shows the *J–V* characteristics of electron–dominated device of **X-PDI** and $PC_{61}BM$ without ZnO NP. The electron mobility of **Br-PDI** is 1.08×10^{-3} cm^2 V^{-1} s^{-1}, which is significantly better than that of **H-PDI** or **F-PDI**, about 10 and 130 times higher, respectively. The electron mobility of **Br-PDI** is in a same order of magnitude as that of $PC_{61}BM$. In fact, electron mobility determined from SCLC follows the same trend of DC σ_0 found for **X-PDI** and $PC_{61}BM$. We also took the **X-PDI** and $PC_{61}BM$ in the fabrication of electron–dominated device with ZnO NP top contact layer. As data shown in Table 3 and figures of Figure 5b and 5d, the electron mobility of **X-PDI** and $PC_{61}BM$ was improved 1.55 ~17 and ~5 times, respectively, comparing with those without ZnO NP top contact layer. Our SCLC measurements have demonstrated that the thin film electron mobility of **Br-PDI** is far more superior to that of **F-PDI**. Since the LUMO energy level of **X-PDI** is not much different from each other, we ascribe the difference of determined electron mobility to the morphology of the thin film, of which the surface roughness was found the lowest in the case of **Br-PDI** (see the following AFM section). In addition, due to the improvement of electron mobility by ZnO NP, we expect that adopting ZnO NP as CBL in **Br-PDI** or $PC_{61}BM$ PVSCs can greatly decrease the series resistance (R_s) and largely enhance the fill factor (FF).

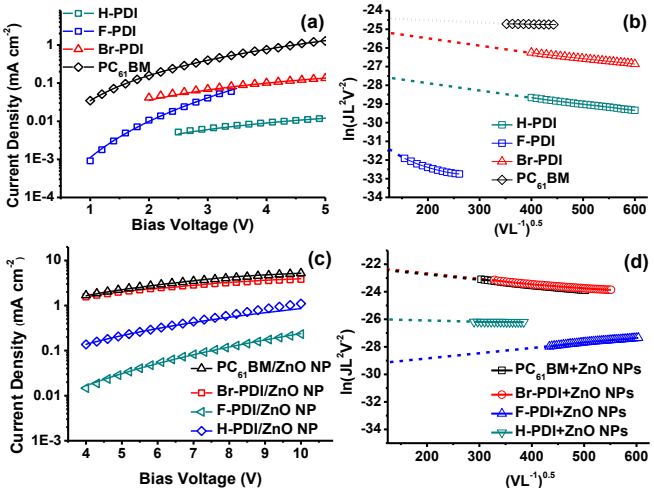

Fig 5 The effect of ZnO NPs top contact layer on electron transport property of **X-PDI** and $PC_{61}BM$. The dark J–V characteristics of devices without ZnO NPs (a, b) and with ZnO NPs (c, d).

Thin film surface morphology of X-PDI, $PC_{61}BM$, and ZnO NP

To investigate the changes in morphology of **X-PDI** solution spin-coated $MAPbI_3$ perovskite films, atomic force microscopy (AFM) measurements were performed in tapping mode. A two-step sequential deposition method was used to prepare high-quality $MAPbI_3$ perovskite film, and its preparation details can

View Article Online
DOI: 10.1039/C7TA02617J

be found in our previous work.[35,36] **X-PDI** or $PC_{61}BM$ chloroform solution was spin-coated on the perovskite substrate. As shown in Figure 6a, 6b, 6c, and 6d, an inhomogeneous surface morphology with high root-mean-square (RMS) roughness as high as 18.8 and 25.4 nm was observed for **H-PDI** and **F-PDI**, respectively. Notably better thin films with lower RMS roughness of 9.5 and 10.4 nm were found for **Br-PDI** and $PC_{61}BM$, respectively. A similar trend of RMS roughness was also found for ZnO NP-covered **X-PDI** or $PC_{61}BM$ thin film (Figure 6e, 6f, 6g, and 6h), i.e., the **F-PDI** sample has the highest surface roughness. Whereas the surface roughness of **H-PDI** sample is in between, the **Br-PDI** sample has the least surface roughness. The **Br-PDI** and $PC_{61}BM$ thin films showed the most flat surface with a height variation less than ~50 nm, which is substantially smaller than ~100 nm and ~150 nm of **H-PDI** and **F-PDI** thin films, respectively. The **F-PDI** has the most uneven and rough surface morphology that may be attributed to the strong molecular interaction due to the fluorine substituent, causing high degree of aggregation in thin film. This is consistent with what we found for the broadening and red-shifting thin film absorption spectrum of **F-PDI** (Figure 2b) and its relatively low solubility in solution.

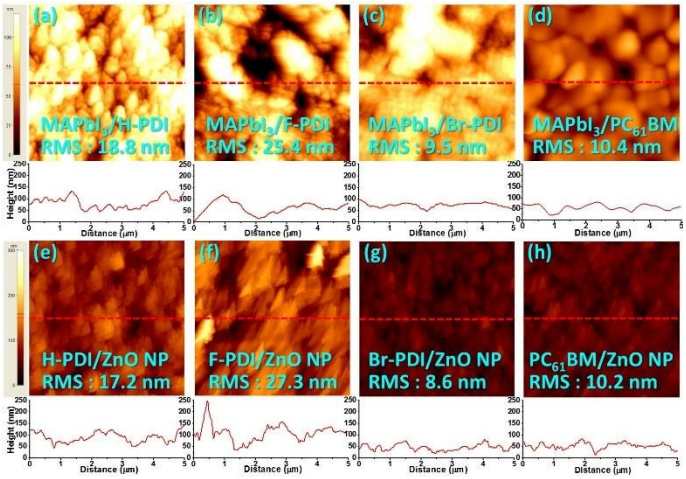

Fig 6 AFM images and height profile of **X-PDI** (a, b, c) or $PC_{61}BM$ (d) and ZnO NP-covered **X-PDI** (e, f, g) or $PC_{61}BM$ (h) thin films, which were prepared from chloroform solution (**X-PDI** layer) and ethanol solution (ZnO NP layer) on ITO/PEDOT:PSS/$MAPbI_3$ substrates. The scanning size of the images is 5 μm × 5 μm. The scale of colour bar is 0-125 nm (for a, b, c, d) and 0-300 nm (for e, f, g, h).

Corresponding SEM images of $MAPbI_3$/**H-PDI**, $MAPbI_3$/**F-PDI**, $MAPbI_3$/**Br-PDI**, and $MAPbI_3/PC_{61}BM$ are shown in Figure 7a, 7b, 7c, and 7d, respectively. Apparently, Figure 7 reals a similar trend of surface roughness in terms of the number of dark domain in the image of **X-PDI** or $PC_{61}BM$ thin films on perovskite active layer.

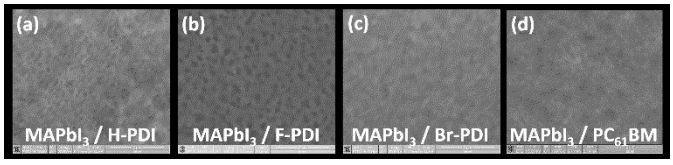

Fig 7 SEM images (~5 x 5 μm) of **X-PDI** or $PC_{61}BM$ thin films on perovskite active layer.

Accordingly, it is foreseeable that **Br-PDI** and $PC_{61}BM$ thin films will have a more extensive contact or a higher surface coverage of perovskite layer, which facilitates a more effective electron transfer across the $MAPbI_3$/ETL interface in PVSCs. Except for **F-PDI**, the ZnO NP CBL or CIL can further enhance such electron transfer and consequent electron transport to the cathode because thin film surface roughness all got more or less reduced.

Charge-trap estimation of $MAPbI_3$/X-PDI interface by photoluminescence

Photoluminescence (PL) is a simple method to study the charge-trap effect between the surface of perovskite film and ETL. Huang and co-workers[37,38] reported that the existence of surface trap states on the perovskite surface or grain boundary could cause band bending close to the surface of the film, lowering the surface bandgap than the bulk one. Therefore, we performed steady-state PL measurement to study the $MAPbI_3$/ETL interface in devices with a configuration of ITO/PEDOT:PSS/$MAPbI_3$/ETL/air. Using an excitation light of 532 nm, which has a power of penetration length shorter than 100 nm much less than the thickness of the perovskite films (~300 nm), we can ensure a surface probing experiment. As shown in Figure 8a, with the incident of excitation light from the air side, the pristine perovskite film showed a PL peaked at 781 nm, which is the same wavelength as the perovskite film covered with **H-PDI** or **F-PDI** but not **Br-PDI** or $PC_{61}BM$. The perovskite film covered with **Br-PDI** or $PC_{61}BM$ exhibited a blue-shifted PL peaked at 774 and 773 nm, respectively. Such PL wavelength difference did not happen, if the excitation light was from ITO side (Figure 8b). Our PL study indicates that both **Br-PDI** and $PC_{61}BM$ passivate the trap states close to the top surface of the perovskite film. Accordingly, both **Br-PDI** and $PC_{61}BM$ have a better interfacial contact (and hence more efficient electron extraction) of perovskite material than **H-PDI** or **F-PDI**.

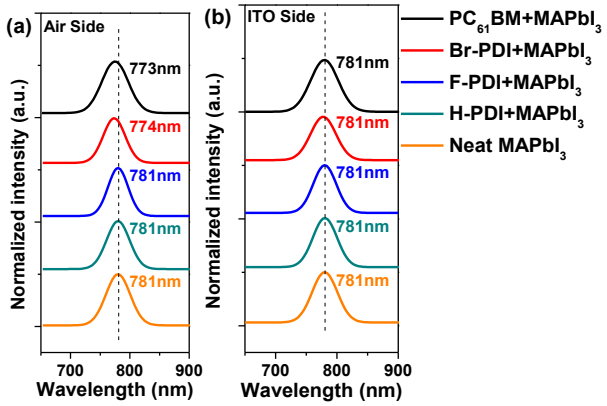

Fig 8 PL spectra of $MAPbI_3$/**X-PDI** and $MAPbI_3/PC_{61}BM$ with excitation light from different incident direction, air side (a) and ITO side (b).

Photovoltaic characterization

The PVSCs with a configuration of ITO/PEDOT:PSS/$MAPbI_3$/**X-PDI** or $PC_{61}BM$/Ag and ITO/PEDOT:PSS/$MAPbI_3$/**X-PDI** or $PC_{61}BM$/ZnO NP/Ag were fabricated and characterized. The detailed fabrication procedures of these devices can be found in the experimental section. The characterization data of all

View Article Online
DOI: 10.1039/C7TA00617J

PVSCs are summarized in Table 4. The corresponding current density (*J*) and voltage (V) plots of PVSCs without ZnO NP CBL are illustrated in Figure 9.

PDI has strong molecular interactions (π-π, F-π, F-F interactions) and hence a serious aggregation in solid state, whereas both **H-PDI** and **Br-PDI** are less serious. The molecular aggregation causes defected thin film, an inhomogeneous and incomplete thin film, of ETL on top of $MAPbI_3$. In this regard, **Br-PDI** outperforms **H-PDI** or **F-PDI** and its device performance is comparable with that of $PC_{61}BM$. Both **Br-PDI** and $PC_{61}BM$ PVSCs show more reasonable R_s, FF, short circuit current (J_{sc}), and hence PCE than those of **H-PDI** and **F-PDI** PVSCs.

Attempting to improve the low PCE of **X-PDI** or $PC_{61}BM$ PVSCs, we introduce solution processed ZnO NP as CBL to overcome or alleviate the problems associated with the ETL. In addition to the data summarized in Table 4, the *J-V* plots of PVSCs with ZnO NP CBL are illustrated in Figure 10a (solar AM 1.5 G irradiation with 100 mW cm^{-2}) and 10b (dark).

Table 4 Summary of the photovoltaic properties of **X-PDI-** and $PC_{61}BM$-based PVSCs

	ETL	PCE_{avg}[a] [%]	V_{oc} [V]	J_{sc} [mA/cm2]	FF [%]	R_{sh} (kΩ cm^2)	R_s (Ω cm^2)	J_0 (mA cm^{-2})	$n_{id,dark}$
W/O ZnO NPs	**H-PDI**	0.66	0.64	6.65	15.4	0.511	274.1	-	-
	F-PDI	~0	0.17	0.12	21.7	51.78	460.6	-	-
	Br-PDI	3.23	0.75	14.64	29.5	0.118	37.60	1.77×10^{-3}	3.19
	$PC_{61}BM$	4.13	0.75	13.76	40.4	0.091	24.52	2.49×10^{-1}	2.47
W/ ZnO NPs	**H-PDI**	7.78	0.73	17.79	59.9	0.887	10.29	2.09×10^{-2}	3.64
	F-PDI	~0	0.06	0.60	20.9	0.049	11.84	4.04×10^{-1}	5.41
	Br-PDI (forward)	10.50	0.83	18.90	66.9	0.269	4.726	1.96×10^{-4}	1.56
	Br-PDI (reverse)	10.20	0.84	18.80	64.6	0.336	6.250	-	-
	$PC_{61}BM$ (forward)	11.07	0.97	17.21	66.3	0.761	6.960	6.15×10^{-4}	1.13
	$PC_{61}BM$ (reverse)	10.24	0.95	16.33	66.0	0.814	6.212	-	-

[a] The average PCE is obtained from over 15 devices.

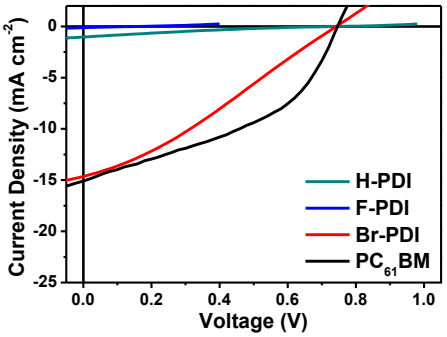

Fig 9 J–V characteristics of X-DPI and $PC_{61}BM$ PVSCs without CBL of ZnO NP under simulated AM 1.5G solar irradiation of 100 mW cm^{-2}.

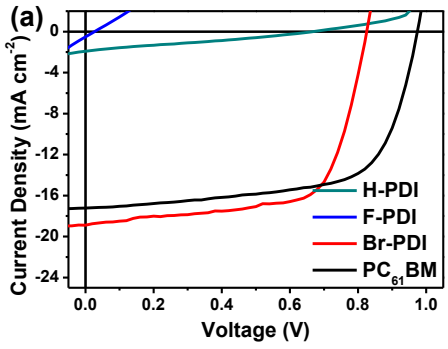

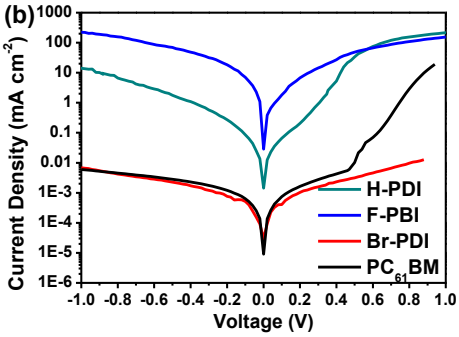

Fig 10 *J–V* characteristics of **X-DPI** and $PC_{61}BM$ PVSCs with CBL of ZnO NP under simulated AM 1.5G solar irradiation (a) and dark (b).

First, as the frontier energy levels of each layer shown in Figure 1a, the stepwise alignment of energy levels from $CH_3NH_3PbI_3$ perovskite layer to Ag cathode facilitates transport and collection of electrons. Energy wise, this is true for each **X-PDI**, $PC_{61}BM$, and ZnO NP. Since the LUMO energy level of each **X-PDI** is lower than that of $PC_{61}BM$; the HOMO energy level of each **X-PDI** is higher than that of $PC_{61}BM$, electron extraction and hole blocking are presumably better for $MAPbI_3$/**X-PDI** than for $MAPbI_3$/$PC_{61}BM$. However, the molecular interaction (aggregation in solid state) and the thin film morphology have a more critical role for the ETL studied herein.

For the devices with $PC_{61}BM$ ETL (as the control PVSL), an average PCE of 4.13% was achieved. For the devices with **X-PDI** ETL, very low average PCE of 0.66% was recorded for **H-PDI** PVSCs and virtually no photovoltaic effect was found for **F-PDI** PVSCs. As evident in spectroscopic and microscopic studies, **F-**

View Article Online
DOI: 10.1039/C7TA00171

As shown from the results, whereas the performance of **F-PDI** devices still remains very poor, PCE of **Br-PDI, H-PDI**, and $PC_{61}BM$ PVSCs with CBL of ZnO NP have notably improved to 10.50%, 7.78%, and 11.07%, respectively. The improvement is comprehensively in all aspects, including V_{oc}, J_{SC}, FF, shunt resistance (R_{sh}), and R_s (Table 4). We can logically infer that the CBL of ZnO NP has an effective function of interspace-filling upon the aggregate domains of **Br-PDI, H-PDI**, and $PC_{61}BM$ thin films. This reduces the direct contact of Ag cathode metal to perovskite material and increases the effective contact area for electron transfer from $MAPbI_3$ perovskite, and the electron mobility (also direct current conductivity) of ETL is also elevated. However, why **F-PDI** PVSCs were not beneficial from the CBL of ZnO NP?

Inspired by the AFM image of the thin film, we have a proposal to explain why CBL of ZnO NP works effectively for **Br-PDI, H-PDI**, and $PC_{61}BM$ but does not work for **F-PDI** devices. As schematically shown in Figure 11a and 11c, an interspace-filling of ETL by ZnO NPs prevents the diffusion of cathode metal (Ag) through the defect of ETL, which will form a direct contact of $MAPbI_3$, facilitating the undesired charge recombination process. Such interspace-filling by ZnO NPs is not effective for **F-PDI**. Due to the large and many interspace between the aggregate domains of **F-PDI**, the solvent (ethanol) used for ZnO NPs goes through the ETL readily and washes away part of perovskite material underneath the interspace of aggregate domains, enabling the direct contact of deposited cathode metal (Ag) (Figure 11b), which is seriously detrimental to the performance of PVSCs.

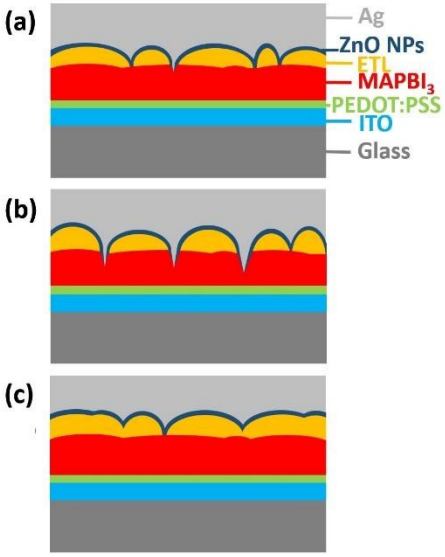

Fig 11 Schematic depict of the cross-sectional view of **H-PDI** (a), **F-PDI** (b), and **Br-PDI** or $PC_{61}BM$ (c) ETLs (yellow) as well as their interspace-filling by ZnO NPs (dark cyan), which prevent the contact of cathode metal Ag (light gray) with $MAPbI_3$ perovskite (red).

The inhibited charge recombination process of **Br-PDI** and $PC_{61}BM$ PVSCs with CBL of ZnO NP gets evidences from a significantly weaker dark current density compared to that of **H-PDI** and **F-PDI** PVSCs with CBL of ZnO NP (Figure 10b). Moreover, the dark *J-V* curves shown in Figure 10b can be modelled using the Shockley diode equation for a single junction device.[39,40] Detailed modelling method can be found in the experimental section. Two key modelling parameters, the reverse saturation current density (J_0) and the ideality factor ($n_{id,dark}$), of all four devices (with CBL of ZnO NP) are summarized in Table 4. Much smaller values of J_0 and $n_{id,dark}$ were obtained for the **Br-PDI** and $PC_{61}BM$ PVSCs compared to that of **F-PDI** devices, whereas J_0 and $n_{id,dark}$ of **H-PDI** devices are in between those of **Br-PDI** and **F-PDI** ones. Such modelling results signify that **Br-PDI** and $PC_{61}BM$ are better materials than **H-PDI** and much better than **F-PDI** for electron selection at the interface of $MAPbI_3$/ETL because of less charge recombination loss. Higher values of V_{oc} observed for **Br-PDI** and $PC_{61}BM$ than **H-PDI** and **F-PDI** PVSCs also can be explained by the less interfacial trap-assisted charge recombination,[41] consistent to the modelling results obtained herein.

It is interesting to know that **Br-PDI** PVSCs always have a higher J_{sc} output than $PC_{61}BM$ PVSCs whether or not devices have ZnO NP (Table 4). Considering the DC conductivity, electron mobility, photoluminescence of perovskite/ETL interface, AFM thin film surface roughness of two materials, we can infer that the better energy alignment, i.e., lower LUMO and HOMO energy levels of **Br-PDI** than $PC_{61}BM$ (see data listed in Table 2) are a main factor. The better energy alignment enables **Br-PDI** to be a more effective material in electron extraction and more efficient in hole-blocking from perovskite material. However, larger energy difference between HOMO (of $MAPbI_3$) and LUMO (of ETL) energy levels renders a higher V_{oc} of $PC_{61}BM$ PVSCs, which offsets the J_{sc} deficiency of the devices. Depending on FF, the PCE of **Br-PDI** and $PC_{61}BM$ PVSCs having ZnO NP CBL is comparable with each other.

Comparing the hysteresis of PVSCs with ZnO NP (Figure 12), ~3% and ~0.5% are the degree of hysteresis effect for **Br-PDI** and $PC_{61}BM$ devices, respectively, based on the calculation of $2 \times (FF_{forward} - FF_{reverse})/(FF_{forward} + FF_{reverse})$ with corresponding data listed in Table 4. We are pleased to know that the hysteresis effect of **Br-PDI** PVSCs is just a little bit more than that of $PC_{61}BM$ PVSCs.

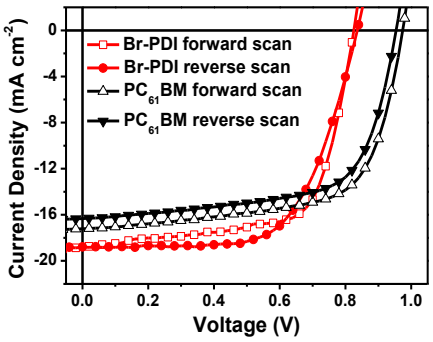

Fig 12 The reverse (1.0 V → - 0.3 V, step 0.02 V, delay time 500 ms) and forward (- 0.3V → 1.0V, step 0.02 V, delay time 500 ms) J–V scans of **Br-PDI and** $PC_{61}BM$ PVSCs with CBL or CIL of ZnO NP.

Conclusions

We have developed and demonstrated three solution processable perylene diimides, i.e., **X-PDI**, **X** = **H**, **F**, or **Br**, as non-fullerene electron accepting and electron transporting

View Article Online
DOI: 10.1039/C7TA04171

materials in inverted PVSCs. Whereas **H-PDI** or **F-PDI** performs unsatisfactorily, our best PVSCs is based on **Br-PDI** exhibiting PCE of 3.23%, which is just a bit shy of 4.13% of fullerene ($PC_{61}BM$) PVSCs. Through a series of physical, spectroscopic, and microscopic studies, we have understood that the low solubility of **F-PDI** is a major factor causing poor quality of the thin film, rendering virtually no photovoltaic effect of **F-PDI**. Although the solubility is better than **F-PDI**, the inferior electron mobility and conductivity compared with those of **Br-PDI** make **H-PDI** PVSCs relatively worse performance. Having the highest solubility, electron mobility, and conductivity among **X-PDI, Br-PDI**-based PVSCs are almost as efficient as $PC_{61}BM$-based PVSCs. Except for **F-PDI**, PCE of PVSCs based on **X-PDI** or $PC_{61}BM$ all get significantly improved to 7.78%, 10.50%, and 11.07%, respectively, once solution processed ZnO NP is included in the PVSCs as a CBL. We infer that the CBL of ZnO NP has a function of interspace-filling on the defect of **H-PDI**, **Br-PDI**, or $PC_{61}BM$ thin film, reducing the direct contact of Ag cathode to the perovskite material. Due to the strong molecular interaction, **F-PDI** aggregates seriously in thin film creating too many and too large defects to be remedied or improved with or without CBL of ZnO NP. Very poor electron mobility and conductivity of **F-PDI** are two other factors devastating its PVSCs.

Experimental

General Instruments

^1H and ^{13}C NMR spectra were recorded on a Brucker AV-400 MHz or AV-500 MHz Fourier transform spectrometer at room temperature. Fast atom bombardment (FB) high resolution mass spectroscopy (HRMS) was performed by Mass Spectroscopic Laboratory as in-house service of the Institute of Chemistry, Academia Sinica. UV-visible absorption spectra were recorded on a Perkin-Elmer lambda 900 spectrometer and Hewlett-Packard 8453 diode array spectrometer for solution and thin film samples, respectively. The PL spectrum was measured by LP920 flash photolysis spectrometer (Edinburgh Instrument, Kirkton Campus, Livingston, England) at room temperature. A 532-nm green laser (Brilliant B laser, Quantel Company, Newbury, Berkshire, UK) was used as the excitation source in PL measurement. The thin film AFM images were obtained by Digital Instrument D3100CL. The thin film SEM images were characterized by FEI Nova NanoLab™ 600 DualBeam (FIB/SEM).

Materials

All chemicals were purchased from Aldrich, Alfa Aesar, Acros, and TCI Chemical Co., and they were used without further purification. Solvents such as dichloromethane (CH_2Cl_2), N-methylpyrrolidinone (NMP), N,N-dimethylformamide (DMF) were distilled after drying with appropriate drying agents. The dried solvents were stored over 4 Å molecular sieves before use. 2,9-bis(2-ethylhexyl)-anthra[2,1,9-*def*:6,5,10-*d',e',f'*]diisoquinoline-1,3,8,10(2*H*,9*H*)-tetraone (**H-PDI**) and 5-bromo-2,9-bis(2-ethylhexyl)-anthra[2,1,9-*def*:6,5,10-*d',e',f'*]diisoquinoline-1,3,8,10(2*H*,9*H*)-tetraone (**Br-PDI**) were synthesized according to the procedures of literature.[29,42] The previously unknown **F-PDI** was synthesized according to the procedures shown in Scheme 1. Patterned ITO-coated glass substrates with a sheet resistance of 15 ohm sq^{-1} were purchased from Ruilong Tech. PEDOT:PSS aqueous solution (Heraeus Clevios™ P VP Al 4083) was purchased from Heraeus. Methylammonium iodide (MAI, CH_3NH_3I, >99.5%) and lead iodide (PbI_2) were purchased from Lumtec and Acros, respectively. The fullerene $PC_{61}BM$ (>99.5%) was purchased from Solenne. Unless otherwise stated, all chemicals were purchased from Sigma-Aldrich and used as received.

Synthesis of 5-fluoro-2,9-bis(2-ethylhexyl)-anthra[2,1,9-*def*:6,5,10-*d',e',f'*]diisoquinoline-1,3,8,10(2*H*,9*H*)-tetraone (F-PDI)

A mixture of **Br-PDI** (2 g, 2.82 mmol), KF (2 g, 34.4 mmol), and DMF (125 mL) was stirred at 130°C for 12 h under argon atmosphere. After the removal of solvent, the residue was subjected to purification by silica gel column chromatography, using CH_2Cl_2/hexane (3/1, v/v) as an eluent, affording **F-PDI** (0.82 g) as a red solid in a yield of 50%. ^1H NMR (400 M Hz, $CDCl_3$) δ ppm: 9.06 (d, 2H, *J* = 8.0 Hz), 8.68 (m, 5H), 8.49 (d, 2H, *J* = 13.6 Hz), 4.17–4.09 (m, 4H), 1.97 (m, 2H), 1.24–1.53 (m, 16H), 0.94 (t, 6H, *J* = 7.6 Hz), 0.89 (t, 6H, *J* = 7.6 Hz). ^{13}C NMR (100 M Hz, $CDCl_3$) δ ppm: 163.62, 163.45, 163.32, 162.57, 162.52, 162.49, 134.35, 133.83, 131.75, 130.97, 130.33, 128.85, 128.61, 128.30, 128.05, 126.29, 126.06, 123.61, 123.31, 123.08, 122.67, 122.00, 121.68, 44.49, 44.44, 44.37, 37.97, 37.94, 30.79, 30.75, 28.71, 28.67, 24.10, 24.07, 23.08, 23.06, 14.08, 10.63, 10.60. MALDI-MS for $C_{41}H_{43}FN_2O_4$, m/z = 646.79, found, m/z = 646.32.

Synthesis of ZnO NPs. ZnO NPs were synthesized by a solution-precipitation process according to literature procedures.[43] Briefly, zinc acetate dihydrate (2.95 g) was dissolved in methanol (125 mL) at room temperature. A potassium hydroxide solution (1.48 g in 65 mL methanol) was then added dropwise within 30 min and stirred for 3 hr at 65 °C. After cooling, the solution was then decanted and the precipitate was washed twice with ethyl acetate and ethanol, respectively. Afterward, ethanol was added to disperse the precipitates and produce ZnO NPs solution with a concentration of 6 mg mL^{-1}. Before use, the ZnO NPs solution was filtered through a 0.45 mm PVDF syringe filter.

Cyclic voltammetry of X-DPI

Using an Electrochemical Analyser BAS C3 operated at a scanning rate of 50 mV s^{-1}, the cyclic voltammetry (CV) was obtained in a tetrabutylammonium hexafluorophosphate (Bu_4NPF_6, 0.1 M) supported CH_2Cl_2 solution containing **X-PDI** or $PC_{61}BM$ (1.0×10^{-3} M) at room temperature. The measurement was conducted with a glassy carbon rod as the working electrode and a platinum wire as the counter electrode. The Ag–Ag^+ (0.1 M of $AgNO_3$ in acetonitrile) was used as the reference electrode. The ferrocene/ferrocenium (Fc/Fc^+) was used as the reference to calibrate the redox potentials. Fc/Fc^+ potential in our CV measurement was +0.10 V relative to Ag-Ag^+. For a thin film CV measurement, **X-PDI** or $PC_{61}BM$ thin film-coated platinum electrode was prepared from a drop-cast

View Article Online
DOI: 10.1039/C7TA02617J

chloroform solution. The CV of **X-PDI** or $PC_{61}BM$ thin film was studied in an anhydrous and nitrogen-saturated solution of acetonitrile containing 0.10 M Bu_4NPF_6. The HOMO and LUMO energy levels of **X-PDI** or $PC_{61}BM$ were calculated based on equations, $E_{LUMO} = -(E_{1/2}^{red1} + 5.10)$ [eV] and $E_{HOMO} = E_{LUMO} - E_g^{op}$ [eV], where E_g^{op} is the optical energy gap corresponding to the absorption onset wavelength of absorption spectra; the energy level of Fc/Fc^+ related to vacuum level is 5.10 eV based on literature reports.[9,31]

Determination of direct current conductivity of X-PDI and $PC_{61}BM$

The **X-PDI** or **$PC_{61}BM$** thin films were prepared by spin-coating method from chloroform solution on an ITO bottom electrode. A layer of Al (100 nm) as top electrode was then deposited through an area (0.2 x 0.5 cm^2) patterned mask in a thermal evaporation chamber under high vacuum (<10^{-6} Torr). The electrical conductivity was analysed on the current-voltage characteristics of the thin film. The DC (direct current) conductivity (σ_0), which is in unit of siemens per metre (S m^{-1}), of the thin film material in such device can be obtained by Claude Pouillet law, $R = L(\sigma_0 A)^{-1}$, where the resistance (R) of a given thin film increases with length (L) but decreases with increasing cross-sectional area (A). The σ_0 is defined as the inverse of resistivity (ρ, in unit of Ω m), i.e., $\sigma_0 = \rho^{-1}$.

Electron mobility determination by SCLC

In the case of a field dependent mobility as described by the Poole-Frenkel effect, the space-charge limited (SCL) current density (J_{SCL}) is given by the modified Mott-Gurney equation,[44] $J_{SCL} = 9\varepsilon_0\varepsilon_r\mu V_{in}^2 \exp(\gamma V^{1/2} L^{-1/2})(8L^3)^{-1}$, where ε_0 is the permittivity of free space (8.854×10^{-12} F m^{-1}); ε_r is the relative dielectric constant of the thin film, which was assigned to be 3; μ is the charge carrier mobility; L is the thickness of the device; V_{in} is the voltage dropped across the sample given by $V_{in} = V - V_{bi} - V_{rs}$, where V is the applied voltage, V_{bi} the built-in voltage, and V_{rs} is the voltage drop due to the series resistance of the contacts; γ is the electric field-activation factor of mobility and accounts for the degree of disorder, particularly the energetic level distribution of the carrier hopping sites in the material. Accordingly, in the region of a log J - log V curve having a slope ~2, the μ can be calculated from the intercept of a $\ln(JL^2 V^{-2})$-$(V L^{-1})^{1/2}$ plot (see Figure 5b and 5d), i.e., $\mu = \exp(\text{intercept}) 8L(9\varepsilon_0\varepsilon_r)^{-1}$. The expression of a field dependent SCL current (SCLC) yields a reasonably good fit to the measured J–V curves of single-carrier devices (see the fitting curves in Figure 5a and 5c).[45]

Fabrication and characterization of perovskite solar cells

ITO-coated glass substrates were cleaned stepwise in detergent, water, acetone, and isopropyl alcohol under ultra-sonication for 20 min each and subsequently pre-treated by UV-ozone for 60 min. The PEDOT:PSS layer (25 nm) was spin-coated on the ITO surface and then annealed at 120 °C for 15 min. The $CH_3NH_3PbI_3$ perovskite layer (~380 nm) was prepared following two-step solution deposition, as described in our previous work.[35,36] Briefly, PbI_2 and MAI were dissolved into DMF–and 2-propanol with concentrations of 450 mg mL^{-1} for PbI_2 and 40 mg mL^{-1} for MAI, respectively. Both solutions and PEDOT:PSS-coated ITO substrates were heated at 100 °C for 10 min before being used. The PbI_2 solution was spun on preheated substrate (5000 rpm for 40 sec) and then annealed at 70 °C for 10 min. The MAI solution was then spun on top of the dried PbI_2 film (6000 rpm for 30 sec), followed by annealing at 100 °C for 2 hr. The **X-PDI** solution (15 mg mL^{-1} in chloroform) was then casted by spin-coating (1000 rpm for 60 sec) on top of the preformed perovskite layers. The thickness of **X-PDI** was near 200 nm. Afterward, ZnO NPs layer (about 10-20 nm) was deposited by spin-coating ZnO NP precursor solution (3000 rpm for 60 sec), then dry in ambient condition without thermal annealing. The opaque Ag cathode (150 nm) was then deposited from thermal evaporator under high vacuum (<10^{-6} Torr). Contributions to the J_{sc} from regions outside the active area were eliminated using illumination masks with an aperture size of 0.12 cm^2. The bulk resistances, R_{sh} and R_s, of samples, were calculated from Ohm's law, $R = V I^{-1}$, with at least ten separate measurements made for each sample.

For the evaluation of the device performance, the devices were illuminated under light intensity of 100 mW cm^{-2} by using a 150 W Class AAA solar simulator (XES-100S1, SAN-EI). The light intensity was determined by using a standard silicon photodiode (Hamamatsu S1133) calibrated by the National Renewable Energy Laboratory. The J–V curves were measured using a Keithley 2400 digital source meter. Unless otherwise stated, the scan rate was set at 0.15 V s^{-1}.

From the J-V characteristics of solar cells in dark circumstance, the dark current densities (J_D) of a solar cell can be estimated according to the thermionic emission model,[39,40] $J_D = J_0[\exp(qV(nkT)^{-1})^{-1}]$, where n is the dark ideality factor, J_0 is the reverse saturation current, q is the elementary charge, and kT is the thermal energy (Boltzmann's constant and temperature). It is well known that the ideality factor of PVSC is normally between 1 and 2.[41] The ideality factor is close to 1 for an ideal trap-free device, while it is closer to or larger than 2 for the case of the deep and dominant charge recombination induced by the trap.

Acknowledgements

This research was support in part by Sustainability Science Research Program of Academia Sinica, Institute of Chemistry of Academia Sinica, National Taiwan University, and the Ministry of Science and Technology of Taiwan.

Notes and references

1 J. Burschka, N. Pellet, S. Moon, R. Humphry-Baker, P. Gao, M. K. Nazeeruddin and M. Grätzel, *Nature*, **2013**, *499*, 316.
2 H. Zhou, Q. Chen, G. Li, S. Luo, T. Song, H.-S. Duan, Z. Hong, J. You, Y. Liu and Y. Yang, *Science*, **2014**, *345*, 542.
3 M. Liu, M. B. Johnston and H. J. Snaith, *Nature*, **2013**, *501*, 395.
4 A. Mei, X. Li, L. Liu, Z. Ku, T. Liu, Y. Rong, M. Xu, M. Hu, J. Chen, Y. Yang, M. Grätzel, H. Han, *Science*, **2014**, *345*, 295.
5 M. Saliba, T. Matsui, J. Seo, K. Domanski, J. P. Correa-Baena, M. K. Nazeeruddin, S. M. Zakeeruddin, W. Tress, A. Abate, A. Hagfeldtd, M. Grätzel, *Energy Environ. Sci.*, **2016**, *9*, 1989.
6 J.-Y. Jeng, Y.-F. Chiang, M.-H. Lee, S.-R. Peng, T.-F. Guo, P. Chen, T.-C. Wen, *Adv. Mater.*, **2013**, *25*, 3727.
7 J. H. Heo, H. J. Han, D. Kim, T. K. Ahnb, S. H. Im, *Energy Environ. Sci.*, **2015**, *8*, 1602.

8 H. Azimi, A. Senes, M. C. Scharber, K. Hingerl, C. J. Brabec, *Adv. Energy Mater.*, **2011**, *1*, 1162.
9 J. Wu, Y. Ma, N. Wu, Y. Lin, J. Lin, L. Wang, C.-Q. Ma, *Org. Electron.*, **2015**, *23*, 28.
10 C. B. Nielsen, S. Holliday, H.-Y. Chen, S. J. Cryer, I. McCulloch, *Acc. Chem. Res.*, **2015**, *48*, 2803.
11 Th. B. Singh, S. Erten, S. Günes, C. Zafer, G. Turkmen, B. Kuban, Y. Teoman, N.S. Sariciftci, S. Icli, *Org. Electron.*, **2006**, *7*, 480.
12 X. Zhan, A. Facchetti, S. Barlow, T. J. Marks, M. A. Ratner, M. R. Wasielewski, S. R. Marder, *Adv. Mater.*, **2011**, *23*, 268.
13 Z. An, J. Yu, S. C. Jones, S. Barlow, S. Yoo, B. Domercq, P. Prins, L. D. A. Siebbeles, B. Kippelen, S. R. Marder, *Adv. Mater.*, **2005**, *17*, 2580.
14 M. Funahashi, A, Sonoda, *Org. Electron.*, **2012**, *13*, 1633.
15 Y. Chen, Y. Feng, J. Gao, M. Bouvet, *J. Colloid Interf. Sci.*, **2012**, *368*, 387.
16 B. A. Gregg, R. A. Cormier, *J. Phys. Chem. B*, **1998**, *102*, 9952.
17 H. Zhang, L. Xue, J. Han, Y. Q. Fu, Y. Shen, Z. Zhang, Y. Li, M. Wang, *J. Mater. Chem. A*, **2016**, *4*, 8724.
18 J. Huang, Z. Gu, L. Zuo, T. Ye, H. Chen, *Solar Energy*, **2016**, *133*, 331.
19 Z. Zhu, J.-Q. Xu, C.-C. Chueh, H. Liu, Z. Li, X. Li, H. Chen, A. K.-Y. Jen, *Adv. Mater.* **2016**, *28*, 10786.
20 Z.-G. Zhang, B. Qi, Z. Jin, D. Chi, Z. Qi, Y. Li, J. Wang, *Energy Environ. Sci.*, **2014**, *7*, 1966.
21 J. Min, Z.-G. Zhang, Y. Hou, C. O. R. Quiroz, T. Przybilla, C. Bronnbauer, F. Guo, K. Forberich, H. Azimi, T. Ameri, E. Spiecker, Y. Li, C. J. Brabec, *Chem. Mater.*, **2015**, *27*, 227.
22 S. S. Kim, S. Bae, W. H. Jo, *RSC Adv.*, **2016**, *6*, 19923.
23 P.S. Mbule, T.H. Kim, B.S. Kim, H.C. Swart, O.M. Ntwaeaborwa, *Solar Energy Mater. Solar Cells*, **2013**, *112*, 6.
24 Y. Jouane, S. Colis, G. Schmerber, P. Kern, A. Dinia, T. Heisera, Y.-A. Chapuis, *J. Mater. Chem.*, **2011**, *21*, 1953
25 O. M. Ntwaeaborwa, R. Zhou, L. Qian, S. S. Pitale, J. Xue, H.C. Swart, P.H. Holloway, *Physica B*, 2012, 407, 1631.
26 C.-Y. Chang, K.-T. Lee, W.-K. Huang, H.-Y. Siao, Y.-C. Chang, *Chem. Mater.*, **2015**, *27*, 5122.
27 C.-Y. Chang, W.-K. Huang, Y.-C. Chang, *Chem. Mater.*, **2016**, *28*, 6305.
28 C.-Y. Chang, W.-K. Huang, Y.-C. Chang, K.-T. Lee, C.-T. Chen, *J. Mater. Chem. A*, **2016**, *4*, 640.
29 L. Zhang, L. Wang, G. Zhang, J. Yu, X. Cai, M. Teng, Y. Wu, *Chin. J. Chem.* **2012**, *30*, 2823.
30 C.-W. Ge, C.-Y. Mei, J. Ling, J.-T. Wang, F.-G. Zhao, L. Liang,H.-J. Li, Y.-S. Xie, W.-S. Li, *Polym. Sci. Part A Polym. Chem.*, **2014**, *52*, 1200.
31 J. Yi, Y. Ma, J. Dou, Y. Lin, Y. Wang, C.-Q. Ma, H. Wang, *Dyes Pigments*, **2016**, *126*, 86.
32 L. Perrin, P. Hudhomme, *Eur. J. Org. Chem.* **2011**, *2011*, 5427.
33 R. Mercadantea, M. Trsicas, J. Duffb, R. Aroca, *J. Mol. Struct.-Theochem.*, **1997**, *394*, 215.
34 J. D. Fernandesa, P. H. B. Aoki, R. F. Arocac, W. D. M. Juniora, A. E.-d. Souzaa, S. R. Teixeiraa, M. L. Braungera, C.-d. A. Olivatia, C. J. L. Constantino, *Mater. Res.*, **2015**, *18(Suppl 2)*, 127.
35 C.-Y. Chang, W.-K. Huang, J.-L. Wu, Y.-C. Chang, K.-T. Lee, C.-T. Chen, *Chem. Mater.*, **2016**, *28*, 242.
36 C.-Y. Chang, Y.-C. Chang, W.-K. Huang, W.-C. Liao, H. Wang, C. Yeh, B.-C. Tsai, Y.-C. Huang, C.-S. Tsao, *J. Mater. Chem. A*, **2016**, *4*, 7903.
37 C. Sun, Z. Wu, H.-L. Yip, H. Zhang, X.-F. Jiang, Q. Xue, Z. Hu, Z. Hu, Y. Shen, M. Wang, F. Huang, Y. Cao *Adv. Energy Mater.*, **2016**, *6*, 1501534.
38 Y. Shao, Z. Xiao, C. Bi, Y. Yuan, J. Huang, *Nat. Comm.*, **2014**, *5*, 5784.
39 X. Li, H. Zhu, K. Wang, A. Cao, J. Wei, C. Li, Y. Jia, Z. Li, X. Li, D. Wu, *Adv. Mater.*, **2010**, *22*, 2743.
40 X. Yu, X. Shen, X. Mu, J. Zhang, B. Sun, L. Zeng, L. Yang, Y. Wu, H. He, D. Yang, *Sci. Rep.*, **2015**, *5*, 17371.
41 A. Zekry, G. Eldallal, *Solid-State Electron.*, **1998**, *31*, 91.
42 Á. J. Jiménez, M. Sekita, E. Caballero, M. L. Marcos, M. S. Rodríguez-Morgade, D. M. Guldi, T. Torres, *Chem. Eur. J.*, **2013**, *19*, 14506.
43 D. Liu, T. L. Kelly, *Nat. Photon.*, **2014**, *8*, 133.
44 P. N. Murgatroyd, *J. Phys. D: Appl. Phys.*, **1970**, *3*, 151.
45 L. C. Palilis, M. Uchida, Z. H. Kafafi, *IEEE J. Sel. Top. Quantum Electron.*, **2004**, *10*, 79.

View Article Online
DOI: 10.1039/C7TA02617J

Graphical abstracts

Mono-halogenated perylene diimides as solution-processable electron transporting layer in inverted perovskite solar cells with ZnO nanoparticle cathode buffer layer